We are IntechOpen, the world's leading publisher of Open Access books
Built by scientists, for scientists

5,300
Open access books available

130,000
International authors and editors

155M
Downloads

Our authors are among the

154
Countries delivered to

TOP 1%
most cited scientists

12.2%
Contributors from top 500 universities

WEB OF SCIENCE™

Selection of our books indexed in the Book Citation Index in Web of Science™ Core Collection (BKCI)

Interested in publishing with us?
Contact book.department@intechopen.com

Numbers displayed above are based on latest data collected.
For more information visit www.intechopen.com

Chapter

Challenges in Improving Performance of Oxide Thermoelectrics Using Defect Engineering

Jamil Ur Rahman, Gul Rahman and Soonil Lee

Abstract

Oxide thermoelectric materials are considered promising for high-temperature thermoelectric applications in terms of low cost, temperature stability, reversible reaction, and so on. Oxide materials have been intensively studied to suppress the defects and electronic charge carriers for many electronic device applications, but the studies with a high concentration of defects are limited. It desires to improve thermoelectric performance by enhancing its charge transport and lowering its lattice thermal conductivity. For this purpose, here, we modified the stoichiometry of cation and anion vacancies in two different systems to regulate the carrier concentration and explored their thermoelectric properties. Both cation and anion vacancies act as a donor of charge carriers and act as phonon scattering centers, decoupling the electrical conductivity and thermal conductivity.

Keywords: thermoelectrics, nonstoichiometry, defect, phonon scattering, conductive oxide, charge transport

1. Introduction

The demand for alternate energy of fossil fuel becomes a challenging task for the researcher and scientist. A possible strategy for an alternate energy source is thermoelectric (TE) materials, whereby unwanted heat is changed to useful electrical energy with no harmful emissions compared to other traditional power plants. [1, 2] The performance of a TE materials can be evaluated by the figure of merit, $zT = S^2\sigma T/\kappa$, where σ represents the electrical conductivity, *S* is the Seebeck coefficient, *T* is the temperature, and κ is the thermal conductivity. [3, 4] The high zT can be obtained with high electrical conductivity, high Seebeck coefficient, and low thermal conductivity. However, the correlations between them are complex and cannot be treated independently. [5, 6] For instance, the increase in the carrier concentration, rises the electrical conductivity, drop the Seebeck coefficient, and rise the electronic thermal conductivity. [7] Therefore, the optimization of TE performance is a challenging task.

To date, many innovative TE materials like Bi_2Te_3, PbTe, $CoSb_3$ XNiSn, and SiGe have been commercially applied because of their high performance as compared to other TE materials. [5, 8–12] However, these materials have restricted applications

due to their high price, instability in oxidizing atmospheres, and the most important toxicity. [8, 13–15] Therefore, many studies on alternative TE materials with low cost, high efficiency, and environmentally friendly characteristics have been explored. [16–18] In this relay, oxide materials have been considered as the best alternative, such as layered cobalt oxide ($NaCo_2O_4$), and strontium titanium oxide ($SrTiO_3$) due to their low price, thermal stability, and eco-friendly compatibility. [19, 20] For TE applications, *n*-type and *p*-type materials should be coupled. So it is important to develop high performance both *n*-type and *p*-type materials.

Layered structure *p*-type $NaCo_2O_4$ has been explored and is considered as one of the candidate materials for TE applications. [16, 21] This layered structure contains two layers CoO_2 and Na. The CoO_2 layers play the role of electron source which results in high electrical conductivity, while the layer of Na ions is sandwiched among nearby CoO_2 layers which decreases the thermal conductivity along the stacking direction. [22, 23] Various studies propose that such layered structured CoO_2 exhibits low thermal conductivity with metallic-like electrical conductivity, which is very attractive for TE applications. [16, 24]

Similar to highly studied $NaCoO_2$ TE material, $LiNbO_2$ has a layered configuration in which the NbO_6 trigonal-prismatic layers and Li planes are stacked, as shown in the schematic **Figure 1(a)**. This similarity proposes that $LiNbO_2$ could be a new promising TE material. $LiNbO_2$ is a sub-oxide of the main ($LiNbO_3$), and its Li-intercalated structure $Li_{1-x}NbO_2$ was first explored as a promising superconductor. [25–27] It has also been considered as a potential candidate material for numerous technological applications. [28–31] The removal of Li atoms provide additional holes to the valence band, made up of Nb d_Z^2 states, which affects the oxidation of the Nb-atoms and raises the density of states (DOS) at the Fermi level (just like when holes are introduced into $NaCoO_2$). These Li-vacancies increase the carrier concentration, which will raise the electrical conductivity. Moreover, the intrinsic defects in $Li_{1-x}NbO_2$ would act as a scattering center for thermal conductivity. So, defected $Li_{1-x}NbO_2$ is estimated to be extremely favorable for TE applications because of higher electrical and lower thermal conductivities.

Stoichiometric $SrTiO_3$ has a cubic perovskite structure, where oxygen anions form an octahedron with one Ti^{4+} atom lying at the center as shown in the schematic

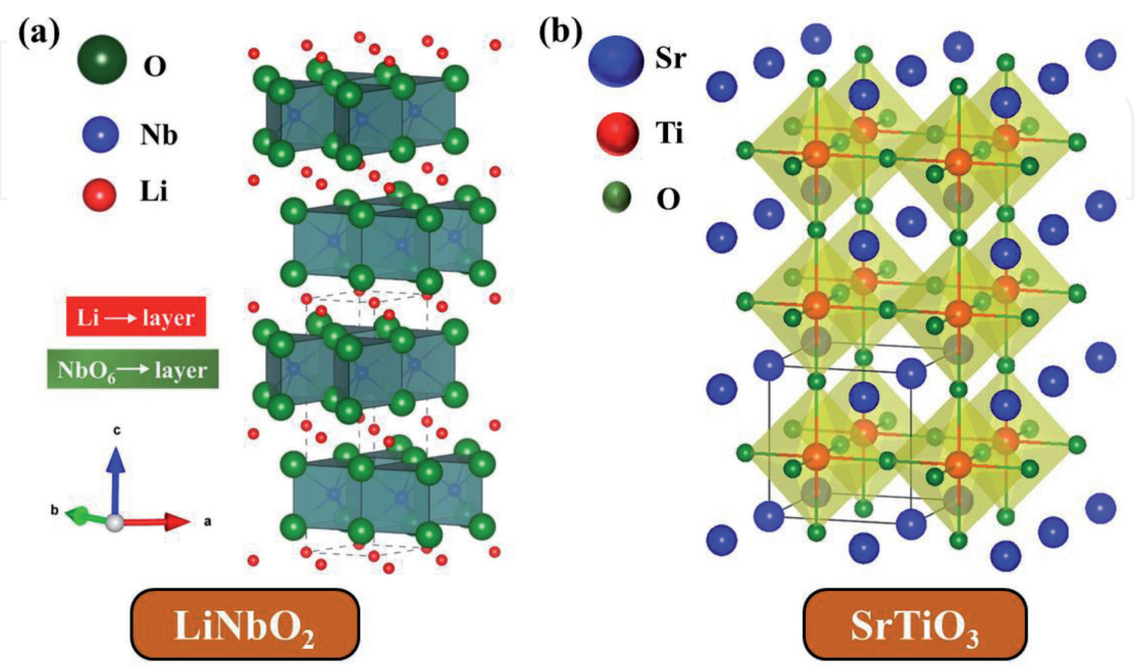

Figure 1.
Schematic illustration of (a) $LiNbO_2$ (b) $SrTiO_3$.

Figure 1(b). $SrTiO_3$ have been studied widely and is considered as one of the favorite *n*-type TE materials due to its high absolute Seebeck coefficient. [32, 33]. Virgin $SrTiO_3$ is considered to be an insulator and with a bandgap of 3.25 eV. [34] To boost the power factor (PF), only the electrical conductivity needs to be increased through appropriate doping on A-site and/or B-site. [19, 35–39]. The role of the oxygen vacancy, which also acts as electron dopants, is very important for TE materials. Besides, creating oxygen vacancies offer a chance to decrease thermal conductivity through phonon scattering without remarkably affecting electrical conductivity. [40–42] The cationic nonstoichiometry and controlling oxygen partial pressure in $SrTiO_3$ can produce cation and oxygen vacancies, which play an important role in the TE performance. To understand the defect chemistry and its consequence on the TE performance, pure $SrTiO_3$ should be considered.

Considering the importance of defects in oxide materials as discussed above, it is important to study cation and anion defect engineering in oxide materials. Here in this chapter we have considered $LiNbO_2$ (*p*-type) and $SrTiO_3$ (*n*-type) with different vacancy concentrations and explore the experimental observations and correlate them with density functional theory (DFT). We elucidate that the defect engineering which may provide a new track for enhancing the TE performance.

2. Cation defect engineering

2.1 Experimental and computational approaches

2.1.1 Preparation of $Li_{1-x}NbO_2$ compounds

Nonstiochiometric $Li_{1-x}NbO_2$ (x = 0–0.6) compounds were prepared by conventional solid-state reaction using commercially available Li_2CO_3, NbO, and Nb_2O_5 with purity level more than 99.99%. First, $Li_{3-y}NbO_4$ was prepared by mixing Li_2CO_3 and Nb_2O_5 (y = 0, 0.015, 0.3, 0.6, 0.9, 1.2, and 1.8) at 1173 K in air for 50 hrs. Next, $Li_{1-x}NbO_2$ (x = 0–0.6) were prepared by mixing $Li_{3-y}NbO_4$ (y = 0, 0.015, 0.3, 0.6, 0.9, 1.2, and 1.8) for corresponding x = (0, 0.05, 0.1, 0.2, 0.4 and 0.6), and NbO in a ratio of 1: 2 for 24 hrs in ethanol. The dried slurries were crushed, sieved, and consulidated by spark plasma sintering (SPS) at 1323 K under 50 MPa for 15 min. [43]

2.1.2 Theoretical calculations of $Li_{1-x}NbO_2$

The electronic structures of $Li_{1-x}NbO_2$ were explored using DFT with the local density approximations. [44] The lattice constants were calculated and all the atomic sites were relaxed till the forces were met to less than 0.01 eV/Å. For Li-vacancies computations various supercells (1x1x1, 1x1x2, 2x2x1, and 2x2x2) were considered. For the TE calculations, the BolzTraP package based on the Boltzmann transport theory and a constant relaxation time were applied. [45, 46] For band structures calculations QE code and the energy dispersion relation $E(n,k)$ as a function of band index n and wave vector k were used.

2.1.3 Characterization of $Li_{1-x}NbO_2$

X-ray diffraction (XRD) analysis was performed by Rigaku D/MAX-2500/PC with Cu Kα emission. The pictographs of the samples were observed by using the scanning electron microscope (SEM, Verios 460 L, FEI). Rectangular specimens were cut for the measurements of the electrical properties using (ZEM-3, ULVAC-RIKO). Temperature-dependent charge transport properties were measured using

HT-Hall, Toyo Corporation, ResiTest 8400. Circular discs were used for thermal diffusivity measurement (DLF-1300, TA instrument). All samples have ≥95% of the theoretical density.

2.2 Results and discussion

Figure 2(a) displays the XRD patterns of all samples. The main peaks of the compounds were indexed according to the $LiNbO_2$ hexagonal structure which can be regarded as alternatively arranged close-packed Li-layers inserted among the two O-Nb-O slabs along the c-axis. [29] In addition to the main peaks, all samples showed small impurity peaks of $LiNbO_3$ and NbO_2. $LiNbO_3$ peaks are expected due to moderate PO_2 level during the consolidation process, which changes the oxidation state from Nb^{3+} to Nb^{5+}. The additional NbO_2 peaks can be described by the following defect reaction (1).

$$2NbO + Li_3NbO_4 \rightarrow 3LiNbO_2 \quad (1)$$

At lower Li-vacancy concentrations, the Li atoms to combine with Nb^{3+} ($[1/3Nb^{5+}+2/3Nb^{2+}]^{3+}$) make $LiNbO_2$. But, at high Li-vacancy concentrations, there are insufficient Li-atoms to react with Nb^{3+} ($[1/3Nb^{5+}+2/3Nb^{2+}]^{3+}$) atoms to form $LiNbO_2$ which turn into the NbO_2 phase. Furthermore, at lower oxygen partial pressure the Nb^{5+} in the Li_3NbO_4 compound is thermally reduced to Nb^{4+} which is the consequence of the NbO_2 phase. Additionally, the Li-vacancies lead to an increase in the repulsive force among the two adjacent oxygen layers which increases the *c*-lattice of the unit cell. In the meantime, the *a* lattice decreases due to the shrinkage of Nb-O bonds in NbO_6 octahedra. The experimental lattice constant shown in the inset **Figure 2(a)** is close to reported work and with our DFT results. [47, 48]

Figure 2(b)-(f) displays the fractured cross-section of $Li_{1-x}NbO_2$ samples. The dense of all the samples support the high relative densities larger than 95%. All grains are homogeneously distributed, no obvious segregations, and are randomly oriented. Moreover, the Li-vacancy concentrations have no significant effects on the size and shape of the grains.

Figure 3(a) shows the temperature-dependent electrical conductivities of $Li_{1-x}NbO_2$ samples. At first, the electrical conductivities of the samples increased with Li-vacancy concentrations, suggesting that more holes are created, as shown in the defect reaction [2]. The decreasing trends in the electrical conductivity

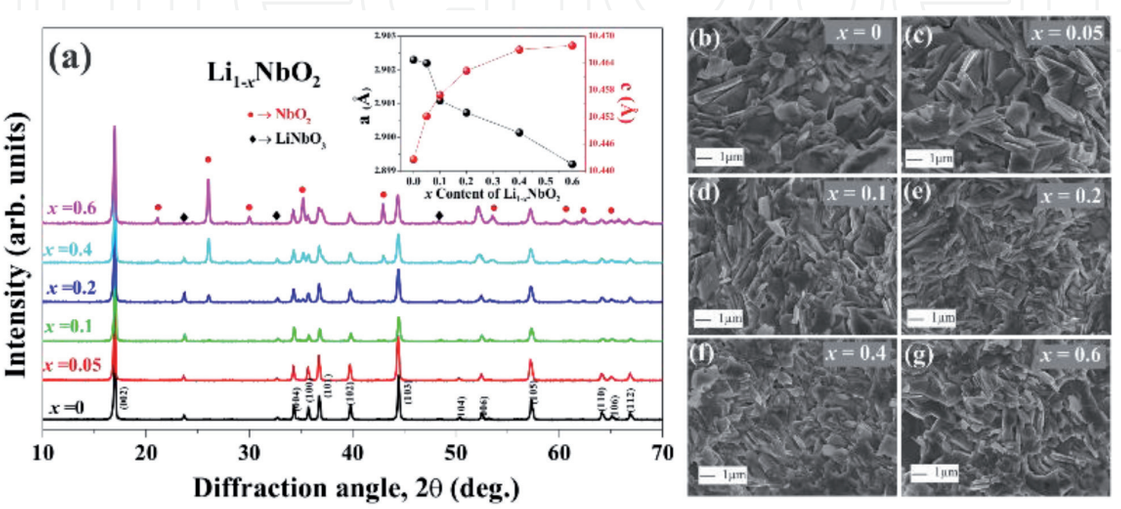

Figure 2.
(a) X-ray diffraction patterns and (b-g) microstructure for $Li_{1-x}NbO_2$ samples. [43].

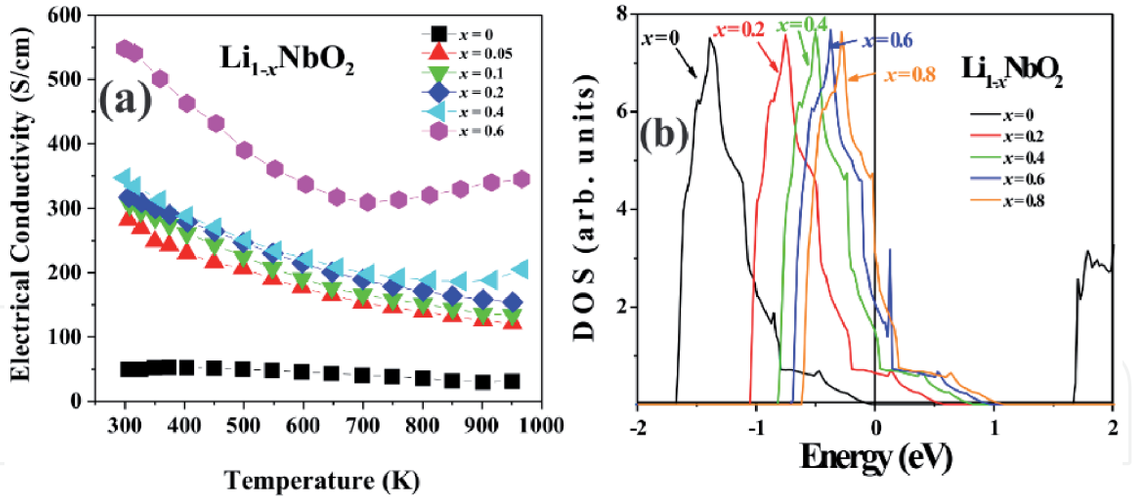

Figure 3.
(a) Temperature dependence of electrical conductivity and (b) calculated electronic density of states of $Li_{1-x}NbO_2$ (x = 0, 0.2, 0.4, 0.6, and 0.6). [43].

measurements with temperature suggesting metallic behavior. However, for higher Li-vacancies concentrations, i.e., $x \geq 0.4$, and at high temperatures the metallic conduction changed to semiconducting-like behavior. For high Li-vacancy concentrations, this transition point is moved to lower temperatures, suggesting that hole creation is inhibited by electrons formed by the replacement of Nb with Li atoms. Above this transition point, the electrical conductivity is governed by electrons which can be described by the defect reactions displayed in Eqs. (3)–(5).

$$Li_2O + Nb_2O_3 \rightarrow 2V_{Li}^{'} + 2h^{\cdot} + 2Nb_{Nb}^{X} + 4O_O^X \tag{2}$$

$$Li_2O + Nb_2O_3 \rightarrow V_{Li}^{'} + Nb_{Nb}^{\cdot\cdot} + Li_{Li}^{X} + Nb_{Nb}^{X} + 4O_O^X \tag{3}$$

$$Li_2O + Nb_2O_3 \rightarrow Nb_{Li}^{\cdot\cdot} + V_{Li}^{'} + e' + Nb_{Nb}^{X} + 4O_O^X \tag{4}$$

$$Li_2O + Nb_2O_3 \rightarrow Nb_{Li}^{\cdot\cdot} + 2e' + Li_{Li}^{X} + Nb_{Nb}^{X} + 4O_O^X \tag{5}$$

To deeply understand the above experimental results DFT calculations were also employed and the electronic structures were calculated. The calculated electronic structure suggests that virgin $LiNbO_2$ has a band-gap of 1.65 eV. It should be noted that DFT-LDA generally miscalculates the band-gap. But, the calculated band-gap in our work is consistent with the reported works. [45] **Figure 3(b)** summarizes the electronic DOS for various holes concentrations. It suggests that virgin $LiNbO_2$ is a semiconductor and suggesting a metallic behavior for holes incorporated samples. Besides, the DOS at the Fermi energy also increases, suggesting that the electrical conductivity of $Li_{1-x}NbO_2$ should increase with increasing holes concentrations.

Figure 4(a) shows the temperature-dependent Seebeck coefficients (S) for all samples. It can be seen that both the calculated and experimentally observed S are very close. The positive sign indicates that holes are the majority carrier which can be connected to the deviation from stoichiometry in the Li- sublattice. [49] The S values of $x \leq 0.1$ samples increase with temperature, showing a degenerately doped semiconductor. Sample with x = 0.2 and at high temperatures the increasing trend in the S values is low suggesting that the hole generation is suppressed by an

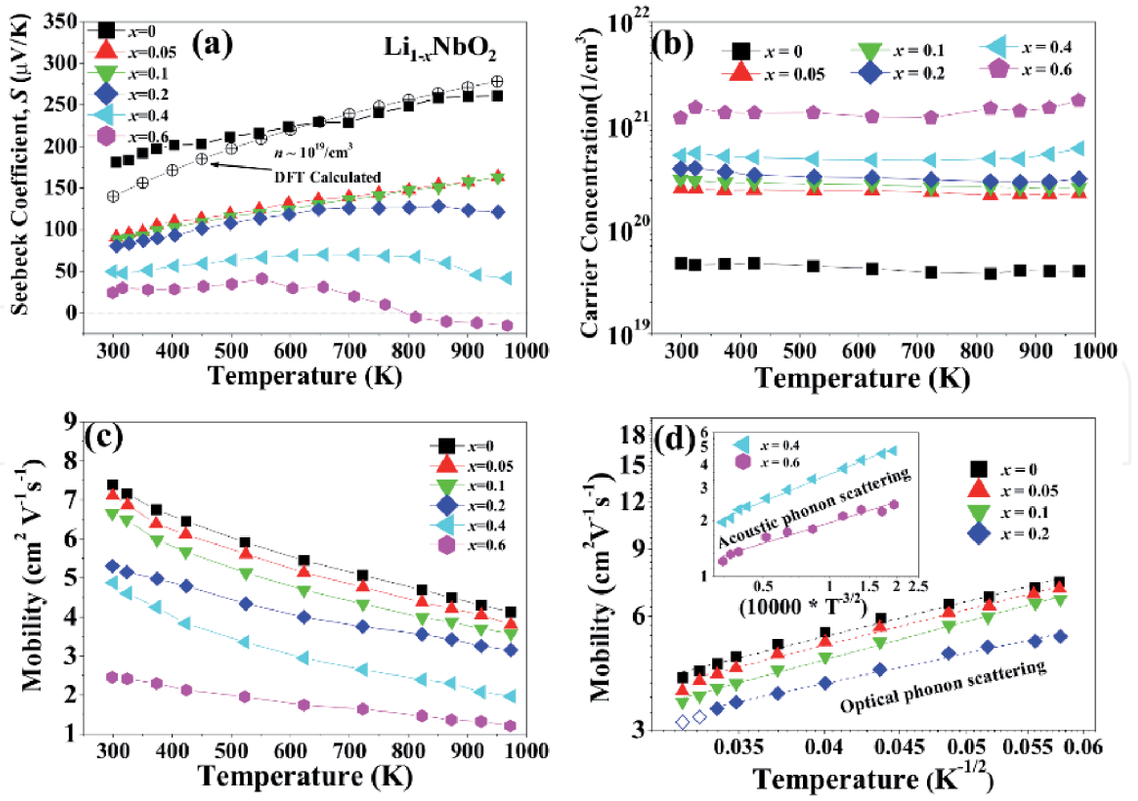

Figure 4.
Temperature dependence of (a) Seebeck coefficient, (b) carrier concentration, (c) carrier mobility, and (d) normalized mobility as a function of $T^{r-1}\left(r=\frac{1}{2}\text{and}-\frac{1}{2}\right)$, *of* $Li_{1-x}NbO_2$. *[43].*

electron. Additional increase in the Li-vacancy concentrations ($x > 0.2$) and at high temperatures, the S values starts decreasing, and finally, a changeover is observed. This changeover from *p*-type to *n*-type could be due to cation disorder which is very similar to the σ-*T* as displayed in **Figure 3(a)**. The behavior could be clearly understood by the defect reaction (2)– (5).

Figure 4(b)-(d) shows the temperature-dependent Hall measurements for all $Li_{1-x}NbO_2$ samples. The obtained by the Hall measurements agreed with the electrical conductivity and Seebeck coefficient data. It can be seen clearly that the carrier concentration increases with the creations of Li-vacancies $\left(2V_{Li}^{'} \rightarrow 2h^{\cdot}\right)$. Samples with lower Li-vacancy concentrations ($x \leq 0.2$) were not influenced by temperature, suggesting degenerately doped behavior. However, high Li-vacancy concentrations ($x \geq 0.4$), and at high temperatures show a slight rise in the carrier concentration. This tendency is similar to the Seebeck coefficients as shown in **Figure 4(a)**. In the case of a degenerately doped *p*-type semiconductor, the Fermi level lies below the valence band maxima (VBM) and the carrier concentration is temperature independent of up to the intrinsic-extrinsic transition temperature. [50] Therefore, it is expected that $Li_{1-x}NbO_2$ is a heavily doped semiconductor. **Figure 4(c)** shows the temperature dependence mobility of nonstoichiometric $Li_{1-x}NbO_2$ compound and the carrier mobility decreases with increasing temperature. Together with the Hall measurements and the defect reactions (2)– (5), it is expected that the tendency in electrical conductivity is directed by mobility in the region holes are dominant and by carrier concentration in the region where electrons are dominant ($x \geq 0.4$ and at high temperature). All samples show negative temperature-dependence carrier mobility, resulting from the phonon scattering ($\mu \propto T^{r-1}$), where $r=-\frac{1}{2},\frac{1}{2}$, and $\frac{3}{2}$ signify acoustic, optical, and ionized impurity phonon scattering, respectively. [51–53] To know the scattering mechanism in $Li_{1-x}NbO_2$, mobilities were re-plotted as a function of T^{r-1} and shown in **Figure 4(d)**. The samples $x \leq 0.2$ shown a linear correlation with $T^{-1/2}$,

suggesting that mobility is dominantly encountered by optical phonon scattering. However, samples with $x \geq 0.4$, as shown in **Figure 4(d)** inset, displayed a linear relationship with $T^{-3/2}$, suggesting that the mobility is encountered by acoustic phonon scattering. The transition mechanism is not clear, however, it could be due to the dominant defect change with Li-vacancies, corresponding to Equations (2) and (3), to Nb replacements for Li sites, corresponding to Eqs. (4) and (5).

Figure 5(a) represents the temperature-dependent total thermal conductivities (κ_{tot}) of $Li_{1-x}NbO_2$ samples. It can be seen that total thermal conductivity is decreased significantly with increasing Li-vacancies. The Wiedemann-Franz relationship was used to estimate the electronic and lattice thermal conductivity as shown in the inset of **Figure 5(a)**. [54] It is found that the main influence on the total thermal conductivity originates from lattice vibrations and decreased substantially with Li-vacancies. This suggests that Li-vacancies act as a scattering center for phonons. However, for higher vacancy concentrations ($x \geq 0.2$), the thermal conductivity increases to some extent. This increase could be due to a change in the scattering mechanism from optical phonon to acoustic phonon by $Nb_{Li}^{\cdot\cdot}$ contribution as described above. This mechanism is schematically illustrated in **Figure 5(b)-(d)**. Therefore, it could be suggested that samples with low Li-vacancies concentrations may have localized

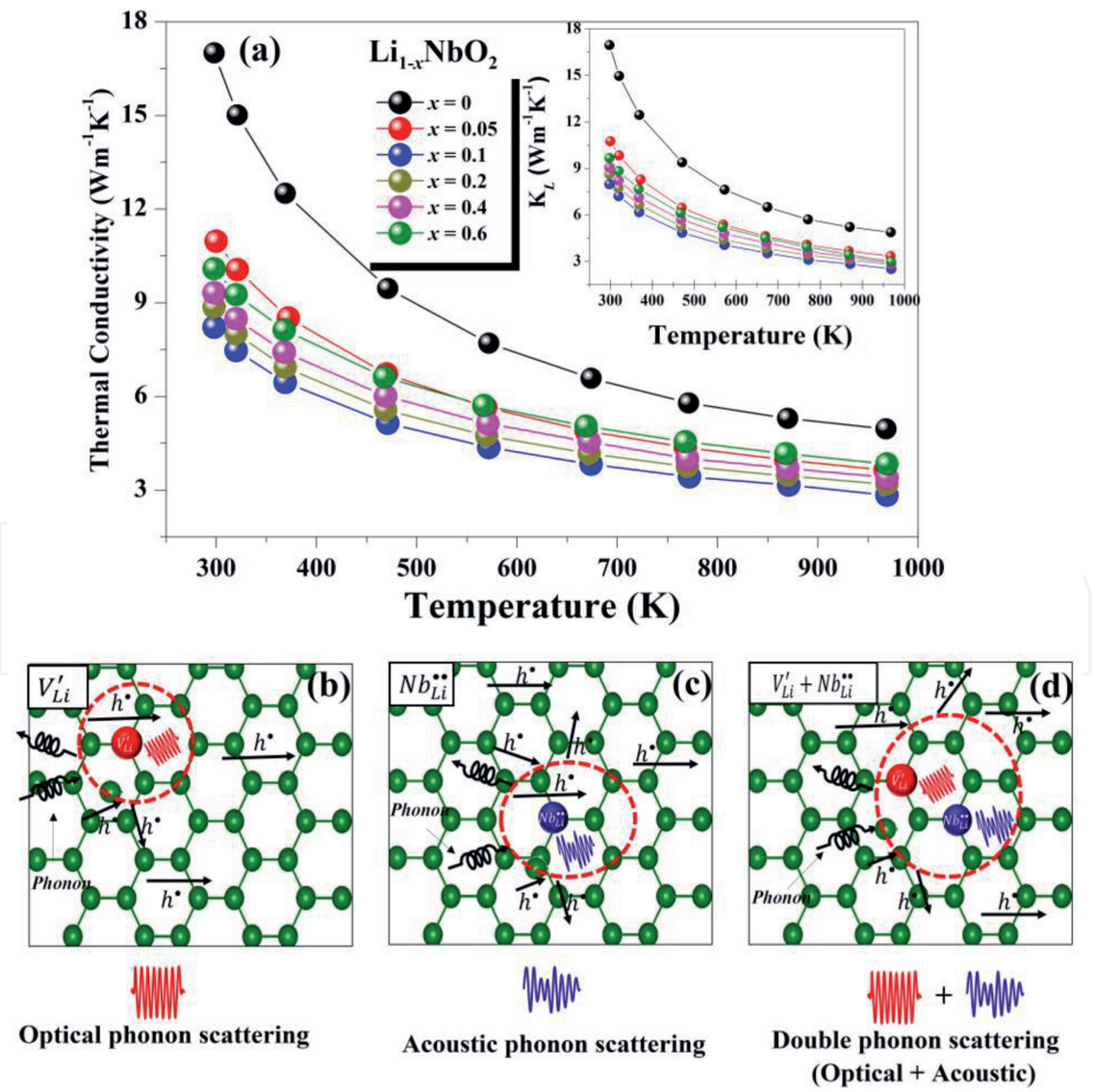

Figure 5.
Temperature-dependent (a) total thermal conductivities for $Li_{1-x}NbO_2$ sample and (b-d) schematic illustration of phonon scattering. [43].

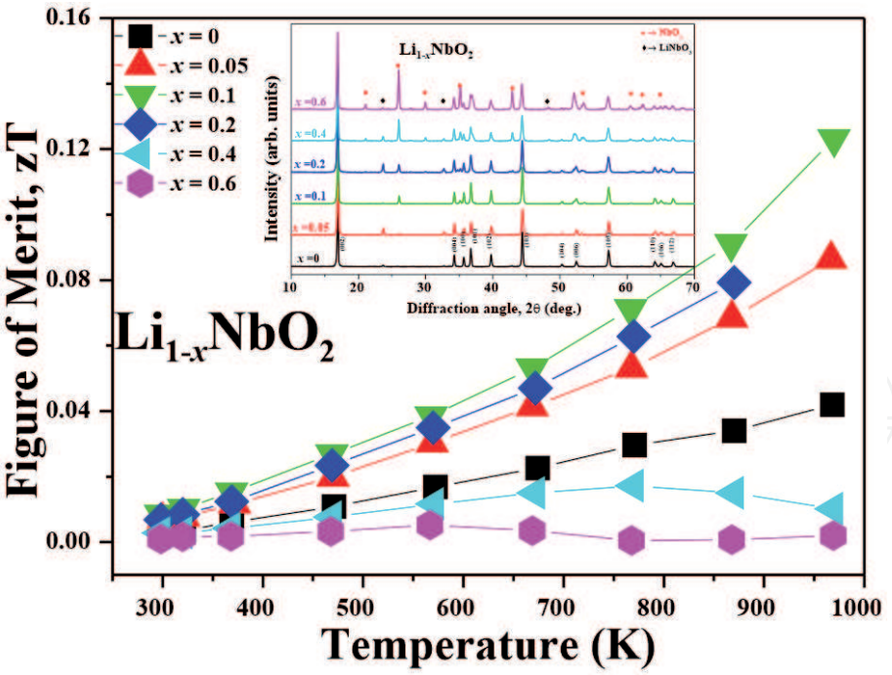

Figure 6.
Temperature dependence of the dimensionless figure of merit of $Li_{1-x}NbO_2$ samples. [43].

double phonon (optical and acoustic phonons), which may play a role as a phonon scattering center, showing a substantial decrease of lattice thermal conductivity. However, with higher Li-vacancies concentrations, the lattice vibration is scattered by a single phonon type of acoustic phonon. Also, the increase in the thermal conductivity could be due to secondary phases [55] as detected in XRD (see **Figure 2(a)**).

The figure-of-merit (zT) for all $Li_{1-x}NbO_2$ samples is presented in **Figure 6**. A substantial improvement in zT is observed in the whole temperature range and reaches a maximum value of 0.125 at 970 K, which is around ~220% (3-times) higher compared to the virgin $LiNbO_2$ sample. The observed tendency suggests that zT could be higher at higher temperatures. The samples after high-temperature measurement were rechecked by XRD and found that all $Li_{1-x}NbO_2$ samples are highly stable as shown in the inset of **Figure 6**. This confirms that all samples are stable and can be utilized as a new promising material for high-temperature TE applications.

3. Anion defect engineering

3.1 Experimental and computational methods

3.1.1 Preparation of $SrTiO_{3-\delta}$

Pristine $SrTiO_3$ samples were synthesized by using conventional solid-state reaction techniques, using TiO_2 and $SrCO_3$ with a purity level higher than 99.9%. The stoichiometric powders were ball-milled for 24 hr. Next, the ball-milled powders were calcined at 1373 K for 3 hrs. The powders were then sieved and pressed into thicknesses of 3 mm. The pressed pellets were sintered at 1573 K for 30 hrs under the air atmosphere. To create an Anion defect in $SrTiO_3$ (Oxygen vacancies), the samples were annealed by allowing 1%H_2/Ar, 5%H_2/Ar, 10%H_2/Ar, and 20%H_2/Ar gases at 1573 K for 30 hrs, and the samples were designated with the prefix "1HAr, 5HAr, 10HAr, and 20HAr", respectively.

3.1.2 Theoretical calculations of $SrTiO_{3-\delta}$

To understand the anion defect engineering in $SrTiO_3$, DFT with the local density approximations were applied and correlated with experimental work. [44, 56] To properly pronounce the electronic band structures of pristine and O-vacancies in $SrTiO_3$, we also considered the LDA + U methodology by selecting the effective on-site Coulomb modification (U = 5.0 eV) is applied to d-orbital electrons in Ti-atom in agreement with the reported works. [57, 58] To compute the oxygen vacancy in $SrTiO_3$, a 2 × 2 × 2 supercell was considered and the BoltzTraP program was used for TE properties. [45, 46].

3.1.3 Charascterization of $SrTiO_{3-\delta}$

For $SrTiO_{3-\delta}$ characterizations, the same techniques were followed as described in section 2.1.3.

3.2 Results and discussion

Figure 7 shows the XRD pattern of the reduced $SrTiO_{3-\delta}$ samples. The XRD patterns of all reduced samples exhibit a single-phase perovskite cubic structure. The lattice constant of the reduced samples was refined through Rietveld refinements. The lattice constant increased with decreasing P_{O_2} levels. The variations in the lattice constant are similar to the reported values. [36, 59] The variations in the lattice constant indicate that during the annealing process, the oxygen in $SrTiO_3$ sublattice combine with H_2 which increases the O-vacancies among the cations, and thus the coulombic repulsion force of cations increases. This leads to a rise in the lattice constant as presented in **Table 1**.

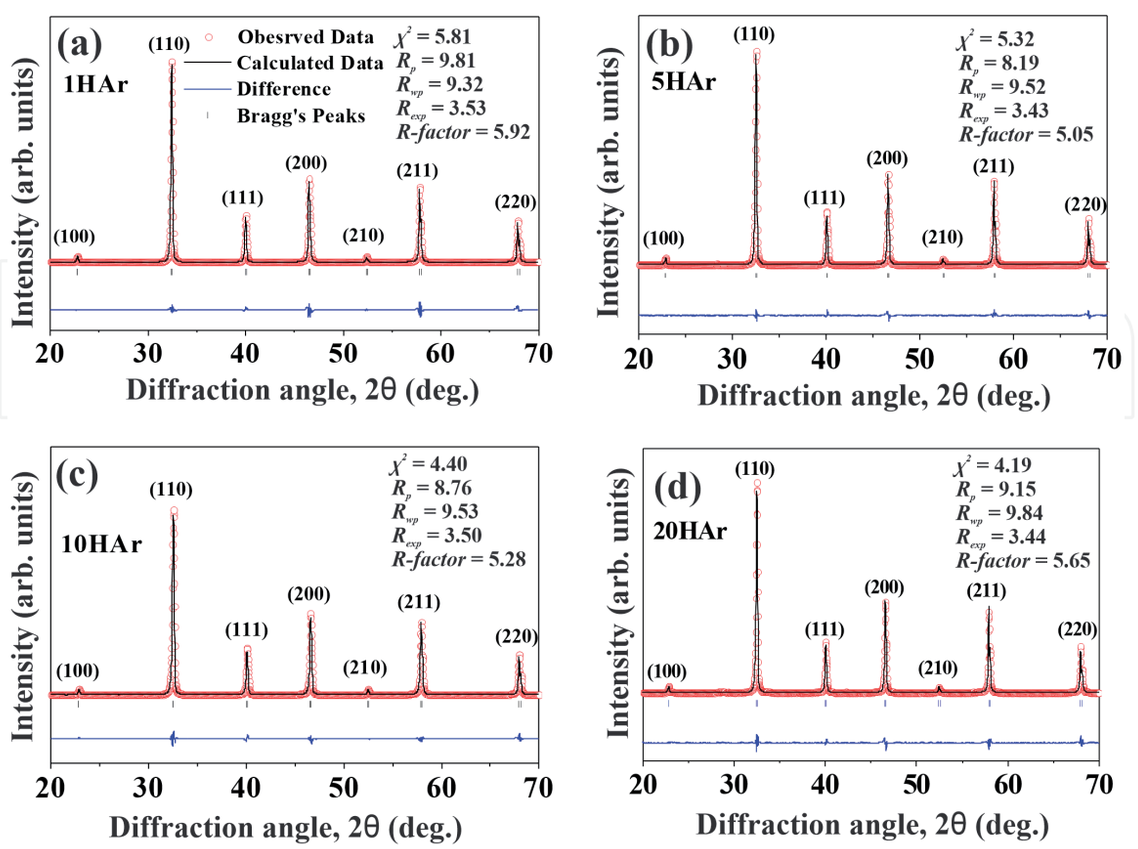

Figure 7.
Refined XRD patterns of oxygen-deficient $SrTiO_{3-\delta}$. ceramics annealed at 1573 K for 30 hrs in (a) 1%H2/Ar (1HAr), (b) 5%H2/Ar (5HAr), (c) 10%H2/Ar (10HAr), and (d) 20%H2/Ar (20HAr) atmospheres [60].

Sample	Lattice parameter (Å)	Carrier concentration ($\times 10^{19}$ cm^{-3})	Oxygen vacancies ($\times 10^{19}$ cm^{-3})	Mobility (cm^{2}V^{-1} s^{-1})	Estimated P_{O_2} (atm)
[1HAr]	3.8991	0.106	0.0530	6.316	2.24×10^{-11}
[5HAr]	3.8999	0.198	0.099	5.373	7.78×10^{-15}
[10HAr]	3.9012	5.24	2.62	4.885	2.23×10^{-23}
[20HAr]	3.9047	10.660	5.33	3.694	3.17×10^{-25}

Table 1.
The carrier concentration, the lattice constant, oxygen vacancies, mobility, and estimated P_{O_2} of $SrTiO_{3-\delta}$ samples. [60].

Figure 8 shows the microstructure of thermally etched $SrTiO_{3-\delta}$ samples in high vacuum conditions. It shows that all samples have similar microstructures, well densified, and support the measured densities>95%. There is no substantial variance in the size and shape of the grains.

Figure 9 displays the high-resolution transmission electron microscopy (HRTEM) of oxygen-deficient $SrTiO_{3-\delta}$ samples. It is interesting to see that the sample reduced under different PO_2 levels shows different reduction levels. In the case of low oxygen-deficient samples, we could not see a clear defective area. However, for the high oxygen-deficient samples, we identify two different kinds of defected areas labeled by A1 and A2 in **Figure 9(c,d)**. The area labeled by A1 denotes the local lattice defect which is due to high oxygen vacancy in the lattice and area A2 shows a different lattice structure from the matrix. It is expected that the

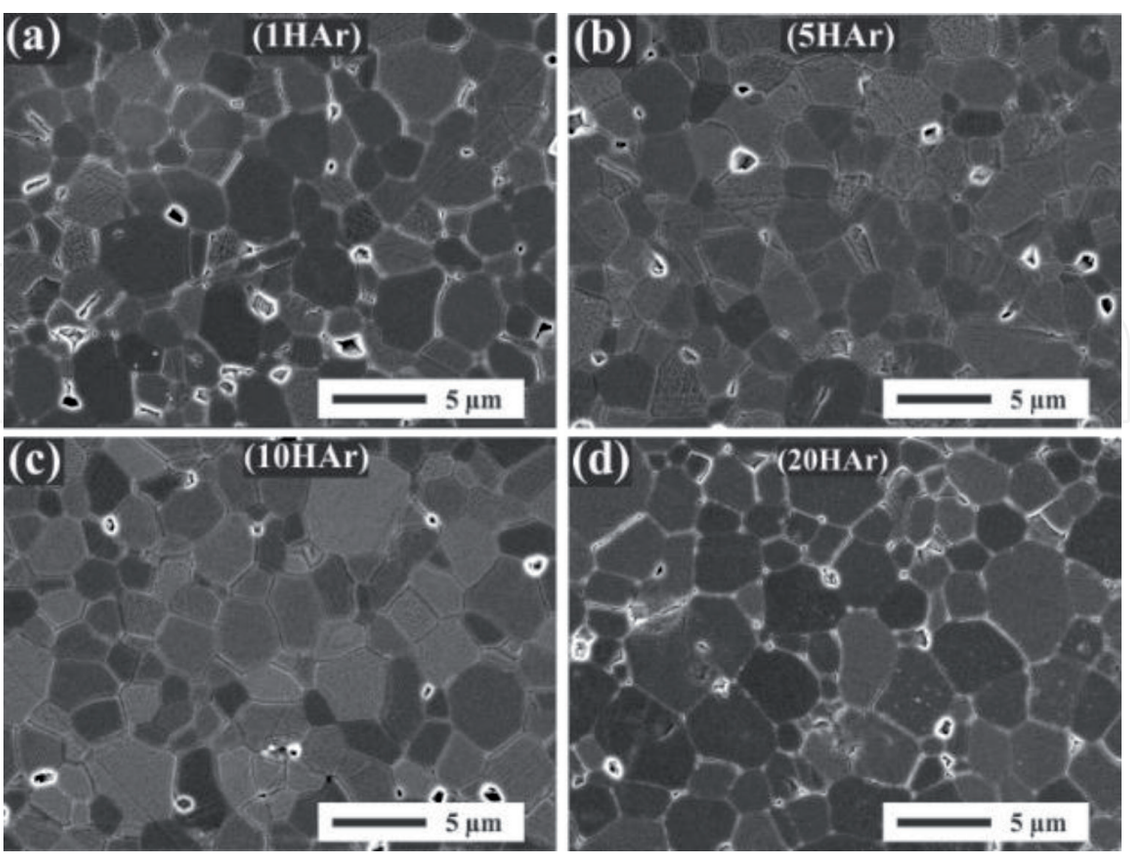

Figure 8.
$SrTiO_{3-\delta}$. ceramics annealed at 1573 K for 30 hrs in (a) 1%H2/Ar (1HAr), (b) 5%H2/Ar (5HAr), (c) 10%H2/Ar (10HAr), and (d) 20%H2/Ar (20HAr) atmospheres [60].

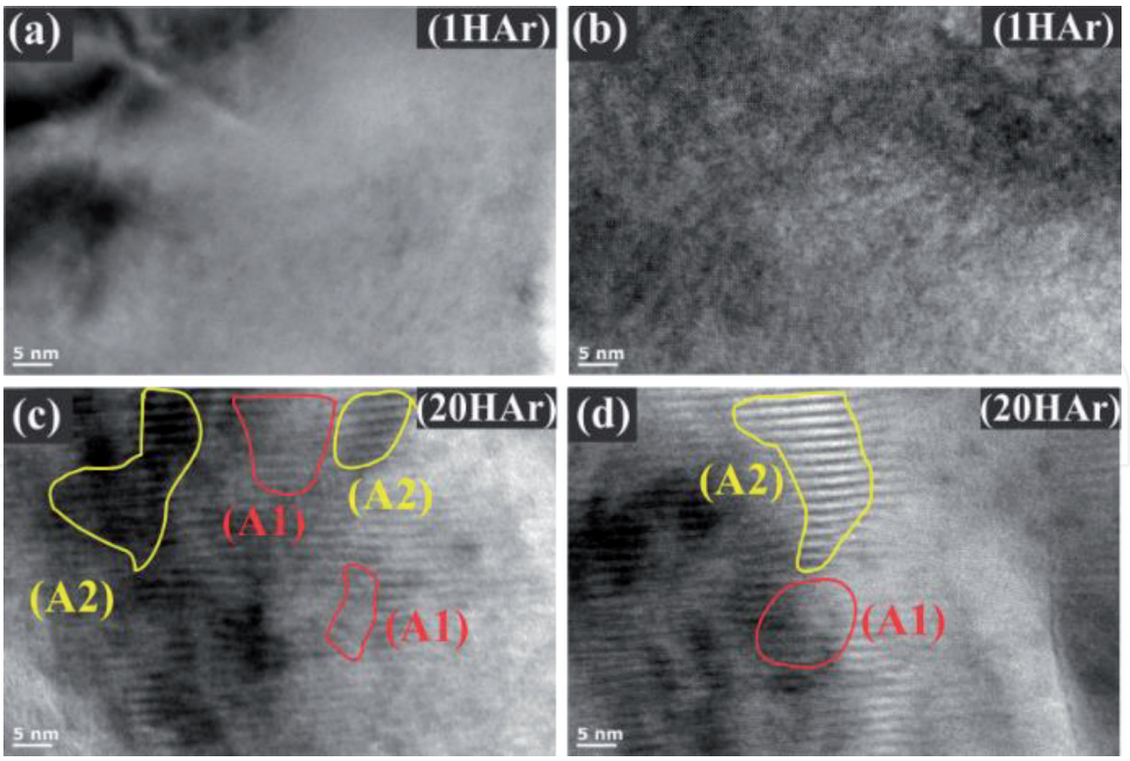

Figure 9.
High-resolution transmission electron microscopy for 1HAr (a, b) and 20HAr (c, d) $SrTiO_{3-\delta}$. [60].

area A2 is probably related to the Ruddlesden-Popper phases $[SrO{\cdot}(SrTiO_3)_n]$ [61], which could be the reason for the metallic conduction in highly reduced samples.

Annealing under a reducing atmosphere at ambient temperature leads to different kinds of defects in materials. Oxygen vacancies could be one of the main defects in the $SrTiO_3$ due to the low formation-energy compared to other atoms in the lattice. Below Eq. (6) shows in the Kröger-Vink notation. [62]

$$O_O^x \leftrightarrow \frac{1}{2}O_2 + V_O^{\cdot\cdot} + 2e' \tag{6}$$

where $V_O^{\cdot\cdot}$ denotes the doubly ionized oxygen vacancy and O_O^x denotes the neutral oxygen that exists on its lattice position. The quasi-free electrons generated by oxygen vacancies was determined using the Hall measurements and then using the free electrons, the oxygen partial pressure PO_2 was estimated using Eq.(7) (See **Table 1**). [63]

$$P_{O_2} = \left(\frac{M 2^{\frac{1}{3}} K_0^{\frac{1}{3}} \exp\left(\frac{-\Delta h_{\mathrm{Re}}}{3 k_B T} \right)}{n_e} \right)^6 \tag{7}$$

where Δh_{Re} represents the enthalpy for reduction, M is the number of oxygen atoms in unit volume (cm^{-3}), k_B is the Boltzmann's constant, K_0 is a constant including an entropy term, n_e is nominal carrier concentration, and T is the annealing temperature.

The observed carrier concentrations in our samples are in the range of 10^{18} to 10^{20}/cm^3, which is a typical range for Mott transition, i.e., insulator–metal transition. This transition can be calculated from the Mott criterion, $n_e^{1/3} a_0 \sim 0.25$, where a_0 is the Bohr radius related to the carrier and n_e which represents the electronic carrier concentration. [64] In the case of 1HAr and 5HAr samples, the calculated Mott transition

is on the boundary of Mott transitions, and 10HAr and 20HAr samples are metallic-like, which supports the temperature-dependency of electrical conductivity.

The temperature-dependent electrical conductivity and Seebeck coefficient of reduced $SrTiO_{3-\delta}$ samples are represented in **Figure 10(a)** and **(b)**. As abovementioned that each O-vacancy produces two electrons through charge neutrality conditions, $n_e \approx 2\left[V_O^{\bullet\bullet}\right]$, and henceforth the carrier concentrations would increase, causing an enhance in the electrical conductivity. [63] Moreover, as shown in **Figure 10(a)** that the electrical conductivities for low reduced samples i.e., 1HAr and 5HAr-annealed are low (0.5 to 2 S/cm, correspondingly) in the entire temperature with semiconducting-like. However, in the case of highly reduced samples (increasing O-vacancies (δ) as shown in **Table 1**) i.e., 10HAr and 20HAr samples, the electrical conductivities are relatively higher (41 and 63 S/cm, correspondingly). This increase of electrical conductivity evidently suggests electron doping due to oxygen vacancy, which is analogous to donor-doped $SrTiO_3$. [65] This would fill the *n*-type conduction band (CB), which evident by the negative sign of the Seebeck coefficient as shown in **Figure 10b**. Additionally, the increase in *n*-type charge carrier from 1HAr to 20HAr is consistent with the electrical conductivity and Seebeck coefficient data.

DFT calculations were also used to understand the effect of O-vacancies in $SrTiO_3$. The electronic band structures of virgin and O-deficient $SrTiO_3$ samples were calculated using DFT + U, and the results are presented in **Figure 10(c)**. Our DFT + U calculated electronic band-gap results suggest that of virgin $SrTiO_3$ at

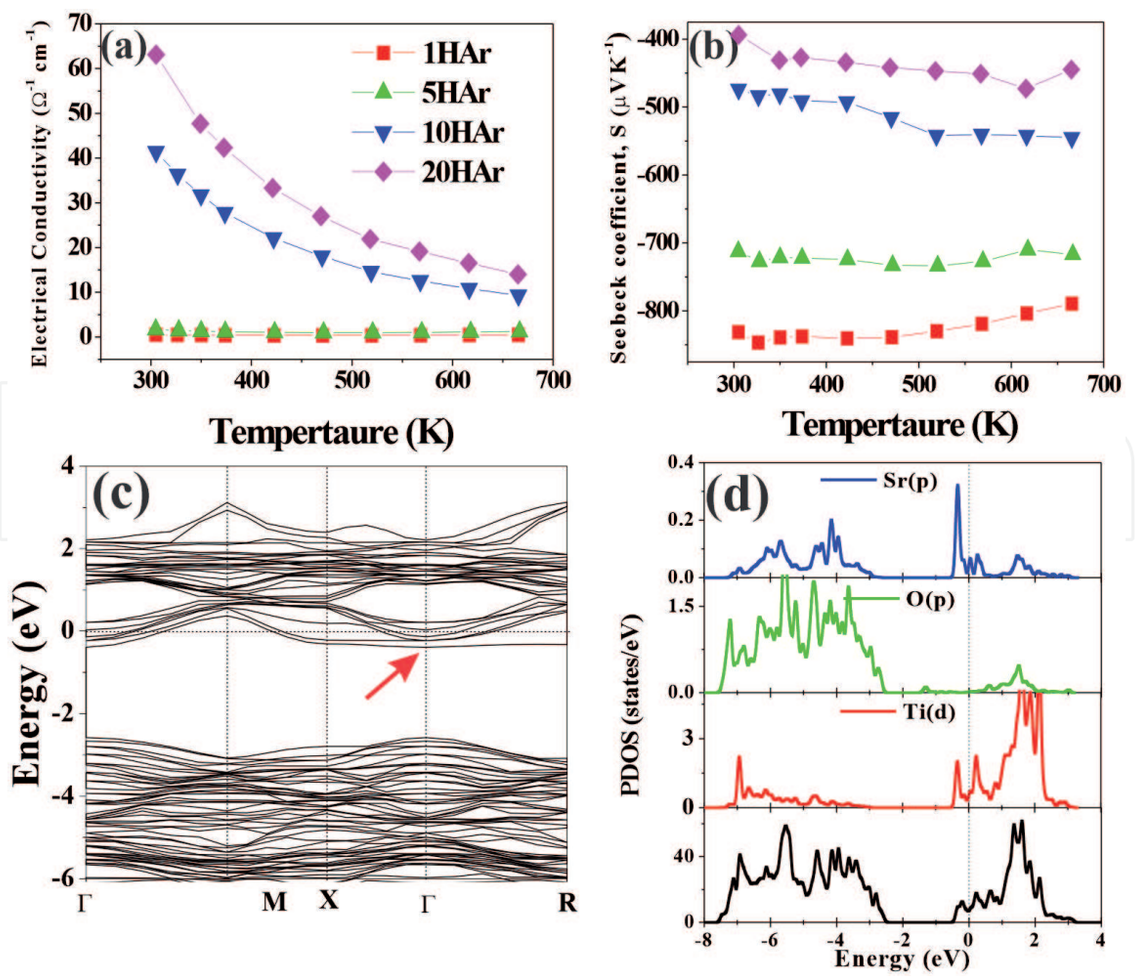

Figure 10.
(a) Temperature-dependent electrical conductivity and (b) Seebeck coefficient of O-deficient $SrTiO_{3-\delta}$, (c) band structure, and (d) total and projected density of states of $SrTiO_{3-\delta}$. [60].

Γ-point is 2.31 eV (1.93 eV), which is close reported work. [34, 66] However, in the case of oxygen-deficient $SrTiO_3$, the electronic band-gap is reduced to 2.18 eV at Γ-point. The band structure calculations show a band below the conduction band, and an electron pocket which can be seen at the Γ- point. Such an electronic pocket suggests electrons in the conduction band, which is largely formed by the Ti-*d* electrons. This electron pocket not only decreases the bandgap but also raises the carrier concentrations that can additionally improve the electrical conductivity of $SrTiO_{3-\delta}$. The projected density of states in **Figure 10(d)** shows that the electron pockets are primarily contributed by the Ti-*d* and Sr-*p* electrons nearby the oxygen vacancy. We also found that at a large O-vacancy concentration, an insulator–metal transition occurs. In addition to this, the charge transfer study also suggests that O-vacancies change the conduction mechanism from nondegenerate to degenerate. We also calculated the room temperature DOS effective mass $\left(m_d^*\right)$ using nondegenerate and degenerate models Eqs. (8) and (9).

$$S = -\frac{k_B}{e}\left[\ln\left(N_c / n_e\right) + A\right] \tag{8}$$

$$S = \frac{8\pi k_B^2}{3eh^2}\left(\frac{\pi}{3n}\right)^{\frac{2}{3}} m_d^* T \tag{9}$$

where k_B represents the Boltzmann constant, h is the Planck constant, n is the carrier concentration, $Nc(\mathrm{T}) = 2\cdot\left[\left(2\pi k_B T m^*\right)/h^2\right]^{3/2}$ is the effective density of states in the conduction band, A is the scattering factor, usually ranges between 0 and 4. By fitting Eq. (8) as shown in **Figure 11a** with A = 1, 2, and 3, it can be seen that the effective mass for low O-vacancies samples suggests a nondegenerate semiconductor. However, the Pisarenko relation fitting Eq. 9 suggests that high O-vacancies samples have degenerate semiconducting like behavior. Furthermore, the DOS effective mass rises with increasing O-vacancies as shown in **Figure 11b**. This increase from 0.43 m_o to 4.4 m_o could be a reason for Hall mobilities reduction as shown in **Table 1**.

Figure 12(a) represents the temperature-dependent thermal conductivity of $SrTiO_{3-\delta}$ samples. This decreasing tendency suggests that O-vacancies act as phonon scattering centers despite their electrical conductivity increased as shown in **Figure 10(a)**. Using Wiedemann-Franz law relation with Lorentz number of

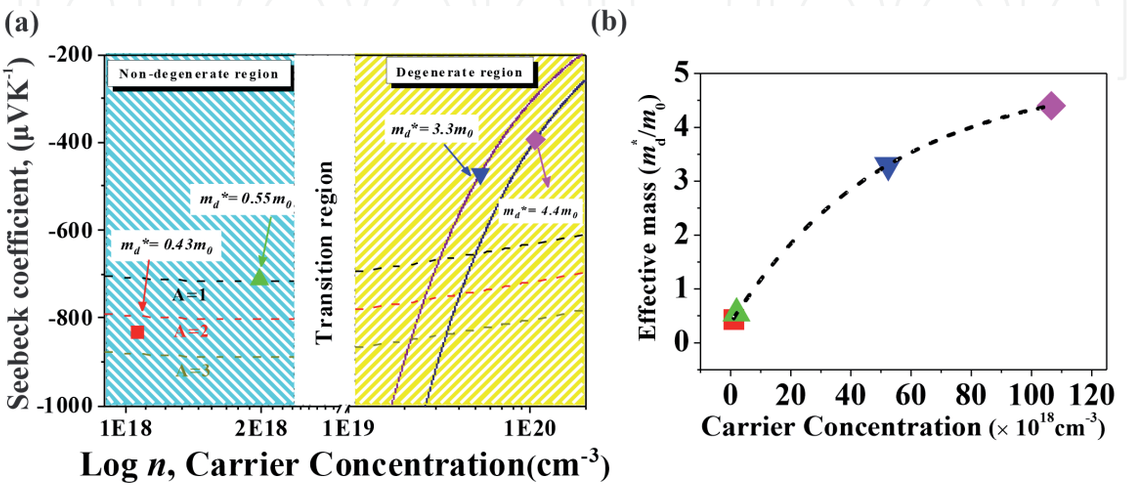

Figure 11.
(a) Seebeck coefficients as a function of carrier concentration: The solid lines represent the estimated Seebeck coefficients using a degenerate semiconducting model and dashed lines for a nondegenerate semiconducting model. (b) DOS effective mass m_d^* resulting from Seebeck coefficient and carrier concentration. [60].

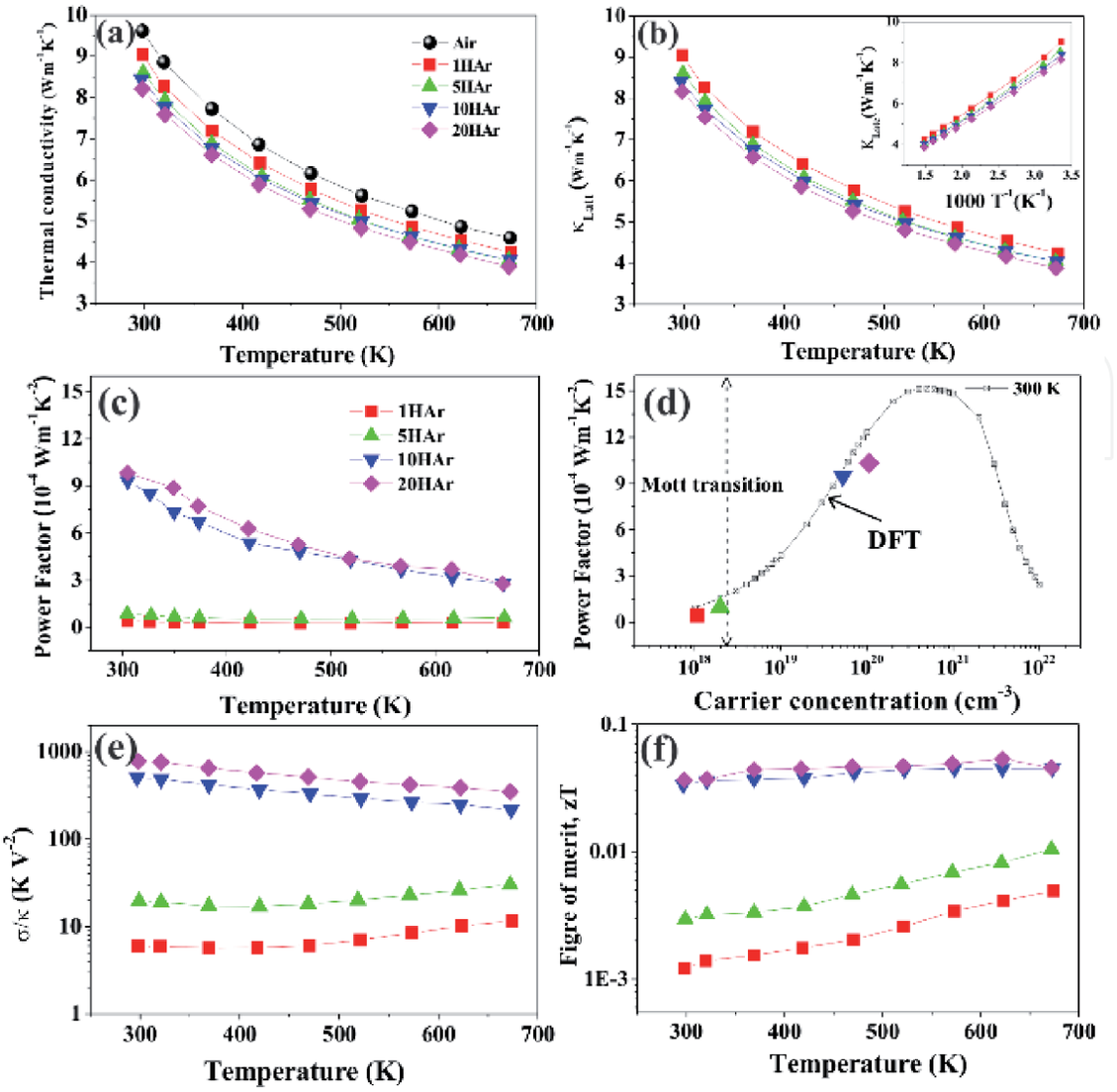

Figure 12.
Temperature-dependent (a) total thermal conductivity, (b) lattice thermal conductivity, (c) power factor, (d) DFT calculated powder factor for various carriers concentrations, (e) temperature-dependent ratio of the electrical to thermal properties (σ/κ), and (d) ZT values of various oxygen-deficient $SrTiO_3$ samples. [60].

(2.45×10^{-8} V^2K^{-2}), the influence of electronic (κ_e) and phononic (κ_L) to total thermal conductivity was calculated and observed that the lattice thermal conductivity is dominant as presented in **Figure 12(b)**. The lattice thermal conductivity was also plotted as a function of T^{-1} as shown in inset **Figure 12(b)**. The linear connection proposes that the lattice thermal conductivity is affected dominantly by Umklapp scattering. [67] Also, one should note that the similar grain sizes as shown in **Figure 8**, suggests that the reduction in thermal conductivity is mainly due to oxygen vacancy rather than grain boundary scattering.

Figure 12(c) illustrates the temperature-dependent PF for various oxygen-deficient $SrTiO_3$ samples. The substantial enhancement in the PF is due to the combination of moderate Seebeck coefficient values and high electrical conductivity. The PF obtained in this work is comparable to the PF obtained in doped-$SrTiO_3$. [65] The DFT calculated PF for various carrier concentrations (10^{18}–10^{22}/cm^3) suggests that the highly reduced $SrTiO_3$ samples would have higher PF as shown in **Figure 12(d)**. [68] Additionally, one of the most remarkable features of this study is the decoupling among electrical and thermal conductivity of $SrTiO_{3-\delta}$ through solely oxygen vacancy as shown in **Figure 12(e)**. This opposite behavior led to a significant increase in the ratio of electrical to thermal conductivity (σ/κ), which is a key motive for TE materials. The complete outcome of oxygen vacancies in

Materials	Type	Maximum zT value	Working temperature (K)	References
Cd-doped $Ca_3Co_4O_9$	*p*	0.35	1000	[69]
Na_xCoO_2	*p*	0.31	800	[70]
Na_xCoO_2/Ag/Au	*p*	0.4–0.5	1000	[71]
$Li_{1-x}NbO_2$	*p*	0.125	970	This work
Nb-doped $SrTiO_3$	*n*	0.165	900	[72]
La-doped $SrTiO_3$ single crystal	*n*	0.27	1073	[73]
Pr-doped $SrTiO_3$	*n*	0.35	773	[74]
$SrTiO_{3-\delta}$	*n*	4.7×10^{-2}	670	This work

Table 2.
The dimensionless figure of merit zT of p*-type and* n*-type oxide thermoelectric materials for comparison.*

the TE materials can be represented by the temperature dependence of the ZT as shown in **Figure 12(f)**. It can be observed that the introduction of oxygen vacancy substantially increases the ZT value of 4.7×10^{-2} for [20HAr] reduced samples at 670 K. Therefore, we suggest that carefully adjusting the oxygen vacancy could be an effective strategy for oxide TE materials.

Table 2 shows that the efforts in the layer-structured cobaltites and $SrTiO_3$ based materials. It shows that significant improvements have been achieved in oxide TE materials, which could be of great interest for power generation applications at high operating temperatures. As compared with other oxides, the materials investigated in this study show relatively low figure of merit (zT), which is because the investigated $Li_{1-x}NbO_2$ and $SrTiO_{3-\delta}$ are pure, undoped materials to understand the mechanism for cation and anion defects effects.

3.3 Conclusion

In conclusion, this work demonstrated that cation and anion vacancies can successfully control the thermoelectric performance of oxide-based thermoelectric materials. These findings suggest that both cation defect and anion defect can be engineered by reducing atmospheres and the defects in oxide thermoelectric materials simultaneously act as a source of charge carriers and phonon scattering centers. This decoupled behavior between electrical conductivity and thermal conductivity can lead to a substantial increase in the thermoelectric performance of oxide materials. The concept applied in this work is generally important and has the possibility of impacting the thermoelectric performance of oxide thermoelectrics and other functional oxide materials.

Acknowledgements

The experimental work was conducted by using the facilities in the Korea Institute of Ceramic Engineering and Technology (KICET). The authors, Jamil Ur Rahman and Soonil Lee are grateful to all colleagues for help and support in the same research group at KICET.

Conflicts of interest

There are no conflicts of interest to declare.

IntechOpen

Author details

Jamil Ur Rahman[1], Gul Rahman[2] and Soonil Lee[3*]

1 Department of Physics, Centre for Materials Science and Nanotechnology, University of Oslo, Sem Saelandsvei, Oslo, Norway

2 Department of Physics, Quaid-i-Azam University, Islamabad, Pakistan

3 School of Materials Science and Engineering/Department of Materials Convergence and System Engineering, Changwon National University, Changwon, Korea

*Address all correspondence to: leesoonil@changwon.ac.kr

IntechOpen

© 2021 The Author(s). Licensee IntechOpen. This chapter is distributed under the terms of the Creative Commons Attribution License (http://creativecommons.org/licenses/by/3.0), which permits unrestricted use, distribution, and reproduction in any medium, provided the original work is properly cited. CC BY

References

[1] G. Mahan, B. Sales, J. Sharp, Thermoelectric materials: New approaches to an old problem. *Physics Today* **50**, 42-47 (1997).

[2] M. S. Dresselhaus *et al.*, New Directions for Low-Dimensional Thermoelectric Materials. *Adv. Mater.* **19**, 1043-1053 (2007).

[3] L.-D. Zhao, V. P. Dravid, M. G. Kanatzidis, The panoscopic approach to high performance thermoelectrics. *Energy Environ. Sci.* **7**, 251-268 (2014).

[4] T. M. Tritt, M. Subramanian, Thermoelectric materials, phenomena, and applications: a bird's eye view. *MRS bull.* **31**, 188-198 (2006).

[5] G. J. Snyder, E. S. Toberer, Complex thermoelectric materials. *Nat. Mater.* **7**, 105-114 (2008).

[6] A. Ioffe, *Semiconductor Thermoelements and Thermoelectric Cooling (London: Infosearch, 1957)*. Google Scholar, pp. 36-38.

[7] Z. Dughaish, Lead telluride as a thermoelectric material for thermoelectric power generation. *Physica B: Condens. Matter* **322**, 205-223 (2002).

[8] G. Nolas, J. Cohn, G. Slack, S. Schujman, Semiconducting Ge clathrates: Promising candidates for thermoelectric applications. *Appl. Phys. Lett.* **73**, 178-180 (1998).

[9] J. M. Song *et al.*, Chemically synthesized Cu2Te incorporated Bi-Sb-Te p-type thermoelectric materials for low temperature energy harvesting. *Scr. Mater.* **165**, 78-83 (2019).

[10] J. S. Yoon *et al.*, High thermoelectric performance of melt-spun $Cu_xBi_{0.5}Sb_{1.5}Te_3$ by synergetic effect of carrier tuning and phonon engineering. *Acta Mater.* **158**, 8 (2018).

[11] N. Van Du *et al.*, X-site aliovalent substitution decoupled charge and phonon transports in XYZ half-Heusler thermoelectrics. *Acta Mater.* **166**, 650-657 (2019).

[12] N. Van Du *et al.*, Synthesis and thermoelectric properties of Ti-substituted (Hf0. 5Zr0. 5) 1-xTixNiSn0. 998Sb0. 002 Half-Heusler compounds. *J. Alloys Compd.* **773**, 1141-1145 (2019).

[13] B. Sales, D. Mandrus, R. K. Williams, Filled skutterudite antimonides: a new class of thermoelectric materials. *Science* **272**, 1325-1328 (1996).

[14] H. Ohta, Thermoelectrics based on strontium titanate. *Mater. Today* **10**, 44-49 (2007).

[15] S. Lee, R. H. T. Wilke, S. Trolier-McKinstry, S. Zhang, C. A. Randall, $Sr_xBa_{1-x}Nb_2O_{6-\delta}$ Ferroelectric-thermoelectrics: Crystal anisotropy, conduction mechanism, and power factor. *Appl. Phys. Lett.* **96**, 031910 (2010).

[16] I. Terasaki, Y. Sasago, K. Uchinokura, Large thermoelectric power in $NaCo_2O_4$ single crystals. *Phys. Rev. B* **56**, R12685 (1997).

[17] T. Kawata, Y. Iguchi, T. Itoh, K. Takahata, I. Terasaki, Na-site substitution effects on the thermoelectric properties of $NaCo_2O_4$. *Phys. Rev. B* **60**, 10584 (1999).

[18] K. Fujita, T. Mochida, K. Nakamura, High-Temperature Thermoelectric Properties of $Na_xCoO_{2-\delta}$ Single Crystals. *Jpn. J. Appl. Phys.,* **40**, 4644-4647 (2001).

[19] S. Ohta, T. Nomura, H. Ohta, K. Koumoto, High-temperature carrier transport and thermoelectric properties

of heavily La- or Nb-doped doped $SrTiO_3$ single crystals. *J. Appl. Phys.* **97**, 34106-034110 (2005).

[20] Y. Wang, N. S. Rogado, R. J. Cava, N. P. Ong, Spin entropy as the likely source of enhanced thermopower in $Na_xCo_2O_4$. *Nature* **423**, 422-425 (2003).

[21] K. Takada *et al.*, Superconductivity in two-dimensional CoO_2 layers. *Nature* **422**, 53-55 (2003).

[22] M. Roger *et al.*, Patterning of sodium ions and the control of electrons in sodium cobaltate. *Nature* **445**, 631-634 (2007).

[23] H. Nakatsugawa, K. Nagasawa, Evidence for the two-dimensional hybridization in $Na_{0.79}CoO_2$ and $Na_{0.84}CoO_2$. *J. Solid State Chem.* **177**, 1137-1145 (2004).

[24] K. Takahata, Y. Iguchi, D. Tanaka, T. Itoh, I. Terasaki, Low thermal conductivity of the layered oxide (Na,Ca)Co_2O_4: Another example of a phonon glass and an electron crystal. *Phys. Rev. B* **61**, 12551 (2000).

[25] E. G. Moshopoulou, a. J. J. C. P. Bordet, Superstructure and superconductivity in $Li_{1-x}NbO_2$ (x≈0.7) single crystals. *Phys. Rev. B* **59**, 9590-9599 (1999).

[26] N. Kumada, S. Watauchi, I. Tanaka, N. Kinomura, Superconductivity of hydrogen inserted $LiNbO_2$. *Mater. Res. Bull.* **35**, 1743-1746 (2000).

[27] E. R. Ylvisaker, W. E. Pickett, First-principles study of the electronic and vibrational properties ofLiNbO2. *Phys. Rev. B* **74**, 075104 (2006).

[28] M. J. Geselbracht, T. J. Richardson, A. M. Stacy, Superconductivity in the layered compound Li_xNbO_2. *Nature* **345**, 324-326 (1990).

[29] N. Kumada *et al.*, Topochemical reactions of Li_xNbO_2. *J. Solid State Chem.* **73**, 33-39 (1988).

[30] J. D. Greenlee, W. L. Calley, W. Henderson, W. A. Doolittle, Halide based MBE of crystalline metals and oxides. *Phys. Status Solidi C* **9**, 155-160 (2012).

[31] J. U. Rahman *et al.*, The Synthesis and Thermoelectric Properties of *p*-Type $Li_{1-x}NbO_2$-Based Compounds. *J. Electron. Mater.* **46**, 1740-1746 (2017).

[32] T. Okuda, K. Nakanishi, S. Miyasaka, Y. Tokura, Large thermoelectric response of metallic perovskites: $Sr_{1-x}La_xTiO_3$ (0~*x*~0.1). *Phys. Rev. B* **63**, (2001).

[33] J. U. Rahman *et al.*, Grain Boundary Interfaces Controlled by Reduced Graphene Oxide in Nonstoichiometric SrTiO3-δ Thermoelectrics. *Scientific Reports* **9**, 8624 (2019).

[34] K. Van Benthem, C. Elsässer, R. French, Bulk electronic structure of $SrTiO_3$: Experiment and theory. *J. Appl. Phys.* **90**, 6156-6164 (2001).

[35] H. Ohta, K. Sugiura, K. Koumoto, Recent progress in oxide thermoelectric materials: *p*-type $Ca_3Co_4O_9$ and *n*-type $SrTiO_3$. *Inorg. Chem.* **47**, 8429-8436 (2008).

[36] H. Muta, K. Kurosaki, S. Yamanaka, Thermoelectric properties of reduced and La-doped single-crystalline $SrTiO_3$. *J. Alloys Compd.* **392**, 306-309 (2005).

[37] Y. Cui *et al.*, Thermoelectric Properties of Heavily Doped *n*-Type $SrTiO_3$ Bulk Materials. *J. Electron. Mater.* **38**, 1002-1007 (2009).

[38] S. R. Sarath Kumar, A. I. Abutaha, M. N. Hedhili, H. N. Alshareef, Effect of oxygen vacancy distribution on the thermoelectric properties of La-doped $SrTiO_3$ epitaxial thin films. *J. Appl. Phys.* **112**, 114104 (2012).

[39] S. Ohta, H. Ohta, K. Koumoto, Grain size dependence of thermoelectric performance of Nb-doped $SrTiO_3$

polycrystals. *J. Ceram. Soc. Jpn.* **114**, 102-105 (2006).

[40] Y. Lin *et al.*, Thermoelectric power generation from lanthanum strontium titanium oxide at room temperature through the addition of graphene. *ACS Applied Mater. Interfaces* **7**, 15898-15908 (2015).

[41] Y. Wang *et al.*, Interfacial thermal resistance and thermal conductivity in nanograined $SrTiO_3$. *Appl. Phys Express* **3**, 031101 (2010).

[42] S. S. Kumar, A. Z. Barasheed, H. N. Alshareef, High temperature thermoelectric properties of strontium titanate thin films with oxygen vacancy and niobium doping. *ACS Applied Mater. Interfaces* **5**, 7268-7273 (2013).

[43] J. U. Rahman *et al.*, Localized double phonon scattering and DOS induced thermoelectric enhancement of degenerate nonstoichiometric $Li_{1-x}NbO_2$ compounds. *RSC Adv.,* **7**, 53255-53264 (2017).

[44] P. Giannozzi *et al.*, QUANTUM ESPRESSO: a modular and open-source software project for quantum simulations of materials. *J. Phys. Condens. Matter* **21**, 395502 (2009).

[45] G. K. Madsen, D. J. Singh, BoltzTraP. A code for calculating band-structure dependent quantities. *Comput. Phys. Commun* **175**, 67-71 (2006).

[46] J. M. Ziman, *Principles of the Theory of Solids*. (Cambridge University Press, 1979).

[47] H. F. Roth, G. Meyer, Z. Hu, G. Kaindl, Synthesis, structure, and *X*-ray absorption spectra of Li_xNbO_2 and Na_xNbO_2 ($x \leq 1$). *Z Anorg. Allg. Chem.* **619**, 1369-1373 (1993).

[48] A. Miura *et al.*, Octahedral and trigonal-prismatic coordination preferences in Nb-, Mo-, Ta-, and W-based ABX_2 layered oxides, oxynitrides, and nitrides. *J. Solid State Chem.* **229**, 272-277 (2015).

[49] K. W. Lee, J. Kuneš, R. T. Scalettar, W. E. Pickett, Correlation effects in the triangular lattice single-band systemLi_xNbO_2. *Phys. Rev. B* **76**, 144513-144511 (2007).

[50] B. G. Streetman, S. Banerjee, *Solid State Electronic Devices*. (Prentice Hall New Jersey, 1980).

[51] B.-L. Huang, M. Kaviany, Ab initio and molecular dynamics predictions for electron and phonon transport in bismuth telluride. *Phys. Rev. B* **77**, 125209 (2008).

[52] H. Kitagawa, A. Kurata, H. Araki, S. Morito, E. Tanabe, Structure and carrier transport properties of hot-press deformed Bi0. 5Sb1. 5Te3. *Phys. Status Solidi (a)* **207**, 401-406 (2010).

[53] T. Zhu *et al.*, Hot deformation induced bulk nanostructuring of unidirectionally grown p-type (Bi, Sb) 2 Te 3 thermoelectric materials. *J. Mater. Chem. A* **1**, 11589-11594 (2013).

[54] C. Kittel, *Introd. Solid State Phys.*, (Wiley, 2005).

[55] N. H. a. M. E. Fine, The Lorenz ratio and electron transport properties of NbO. *J. Appl. Phys.* **52**, 2876 (1981).

[56] W. Kohn, L. Sham, doi: 10.1103/ PhysRev. 140. A1133. *Phys. Rev. A* **140**, 113 (1965).

[57] T. Mizokawa, T. Mizokawa and A. Fujimori. *Phys. Rev. B* **51**, 12 (1995).

[58] S. Okamoto, A. J. Millis, N. A. Spaldin, Lattice relaxation in oxide heterostructures: LaTiO 3/SrTiO 3 superlattices. *Phys. Rev. Lett.* **97**, 056802 (2006).

[59] H. Muta, K. Kurosaki, S. Yamanaka, Thermoelectric properties of rare earth doped $SrTiO_3$. *J. Alloys Compd.* **350**, 292-295 (2003).

[60] J. U. Rahman *et al.*, Oxygen vacancy revived phonon-glass electron-crystal in $SrTiO_3$. *J. Eur. Ceram. Soc.,* **39**, 8 (2019).

[61] C. Xu *et al.*, Formation mechanism of Ruddlesden-Popper-type antiphase boundaries during the kinetically limited growth of Sr rich $SrTiO_3$ thin films. *Scientific reports* **6**, 38296 (2016).

[62] F. Kröger, H. Vink, Relations between the concentrations of imperfections in crystalline solids. *Solid State Phys.* **3**, 307-435 (1956).

[63] S. Lee, G. Yang, R. H. T. Wilke, S. Trolier-McKinstry, C. A. Randall, Thermopower in highly reduced n-type ferroelectric and related perovskite oxides and the role of heterogeneous nonstoichiometry. *Phys. Rev. B* **79**, 134110-134111 (2009).

[64] P. Cox, *Transition metal oxides*. (Oxford University Press, 1992), pp. 158.

[65] A. V. Kovalevsky, A. A. Yaremchenko, S. Populoh, A. Weidenkaff, J. R. Frade, Effect of A-Site Cation Deficiency on the Thermoelectric Performance of Donor-Substituted Strontium Titanate. *J. Phys. Chem. C* **118**, 4596-4606 (2014).

[66] S. Piskunov, E. Heifets, R. Eglitis, G. Borstel, Bulk properties and electronic structure of SrTiO3, BaTiO3, PbTiO3 perovskites: an ab initio HF/DFT study. *Computational Materials Science* **29**, 165-178 (2004).

[67] J. M. Ziman, *Electrons and phonons: the theory of transport phenomena in solids*. (Oxford university press, 1960).

[68] J. Sun, D. J. Singh, Thermoelectric properties of *n*-type $SrTiO_3$. *APL Materials* **4**, 104803 (2016).

[69] S. Butt *et al.*, Enhancement of thermoelectric performance in Cd-doped $Ca_3Co_4O_9$ via spin entropy, defect chemistry and phonon scattering. *J. Mater. Chem. A* **2**, 19479-19487 (2014).

[70] K. Fujita, T. Mochida, K. Nakamura, High-temperature thermoelectric properties of $Na_xCoO_{2-\delta}$ single crystals. *Jpn. J. Appl. Phys.,* **40**, 4644 (2001).

[71] M. Ito, D. Furumoto, Effects of noble metal addition on microstructure and thermoelectric properties of $Na_xCo_2O_4$. *J. Alloys Compd.* **450**, 494-498 (2008).

[72] N. Wang, L. Han, H. He, Y. Ba, K. Koumoto, Effects of mesoporous silica addition on thermoelectric properties of Nb-doped $SrTiO_3$. *J. Alloys Compd.* **497**, 308-311 (2010).

[73] S. Ohta, T. Nomura, H. Ohta, K. Koumoto, High-temperature carrier transport and thermoelectric properties of heavily La-or Nb-doped $SrTiO_3$ single crystals. *J. Appl. Phys.* **97**, 034106 (2005).

[74] A. M. Dehkordi, S. Bhattacharya, J. He, H. N. Alshareef, T. M. Tritt, Significant enhancement in thermoelectric properties of polycrystalline Pr-doped $SrTiO_{3-\delta}$ ceramics originating from nonuniform distribution of Pr dopants. *Appl. Phys. Lett.* **104**, 193902 (2014).